Bad metallic transport in a cold atom Fermi-Hubbard system

Peter T. Brown,[1] Debayan Mitra,[1] Elmer Guardado-Sanchez,[1] Reza Nourafkan,[2] Alexis Reymbaut,[2] Simon Bergeron,[2] A.-M. S. Tremblay,[2,3] Jure Kokalj,[4,5] David A. Huse,[1] Peter Schauß,[1] and Waseem S. Bakr[1,*]

[1]*Department of Physics, Princeton University, Princeton, New Jersey 08544 USA*
[2]*Département de Physique, Institut Quantique, and Regroupement Québécois sur les Matériaux de Pointe, Université de Sherbrooke, Sherbrooke, Québec, Canada J1K 2R1*
[3]*Canadian Institute for Advanced Research, Toronto, Ontario, Canada M5G 1Z8*
[4]*Faculty of Civil and Geodetic Engineering, University of Ljubljana, SI-1000 Ljubljana, Slovenia*
[5]*Jožef Stefan Institute, Jamova 39, SI-1000 Ljubljana, Slovenia*

(Dated: February 27, 2018)

Charge transport is a revealing probe of the quantum properties of materials. Strong interactions can blur charge carriers resulting in a poorly understood "quantum soup". Here we study the conductivity of the Fermi-Hubbard model, a testing ground for strong interaction physics, in a clean quantum system - ultracold ^{6}Li in a 2D optical lattice. We determine the charge diffusion constant in our system by measuring the relaxation of an imposed density modulation and modeling its decay hydrodynamically. The diffusion constant is converted to a resistivity, which exhibits a linear temperature dependence and exceeds the Mott-Ioffe-Regel limit, two characteristic signatures of a bad metal. The techniques we develop here may be applied to measurements of other transport quantities, including the optical conductivity and thermopower.

In conventional materials, charge is carried by quasiparticles and conductivity is understood as a current of these charge carriers developed in response to an external field. For the conductivity to be finite, the charge carriers must be able to relax their momentum through scattering. The central importance of scattering processes is already apparent in the semiclassical Drude theory, which predicts $\sigma = \frac{ne^2}{m^*\Gamma}$, where Γ is the momentum relaxation rate, n is the density, e is an elementary charge, and m^* is the quasiparticle mass. More generally, the Boltzmann kinetic equation in conjunction with Fermi liquid theory provides a detailed description of transport in conventional materials, including two trademarks of resistivity. The first is the Fermi liquid prediction that the temperature-dependent resistivity $\rho(T)$ should scale like T^2 at low temperature [1]. The second, based on the idea that the mean free path of a quasiparticle cannot be less than the lattice spacing, is that the resistivity should not exceed the so called Mott-Ioffe-Regel limit [2, 3].

Strong interactions can modify the above picture in several ways. First, they may destroy quasiparticles, leading to a breakdown of Fermi liquid theory. One signal of this is anomalous scaling of ρ with temperature, including the linear scaling observed in the strange metal state of the cuprates [4] and other anomalous scalings in d- and f- electron materials [5]. Another is the violation of the Mott-Ioffe-Regel limit, which is observed in a wide variety of materials [6]. Second, interactions may also lead to a situation where the momentum relaxation rate alone does not determine the conductivity. This is a radical change, as generalizations of the Drude formula hold for a large class of systems called coherent metals [7], which include Fermi liquids. A variety of approaches have been introduced to understand these anomalous behaviors, including the notion of hidden Fermi liquids [8], marginal Fermi liquids [9], proximity to quantum critical points [10] which has recently led to holographic approaches [11], and many numerical studies of model systems, most notably the Hubbard [12] and $t-J$ [13] models.

Disentangling strong interaction physics from other effects, such as impurities and electron-phonon coupling, is difficult in real materials. Cold atom systems are free of these complications, but transport experiments are challenging due to the finite and isolated nature of these systems. Most fermionic charge transport experiments have focused on either studying mass flow through optically structured mesoscopic devices [14–17] or bulk transport in lattice systems [18–22]. Here, we explore bulk transport in a Fermi-Hubbard system by studying charge diffusion, which is a microscopic process closely related to conductivity. The Nernst-Einstein equation formalizes the relationship between the two according to $\sigma = \chi_c D$, where D is the diffusion constant and $\chi_c = \left(\frac{\partial n}{\partial \mu}\right)\Big|_T$ is the compressibility. This approach takes advantage of the contact nature of atomic interactions. In real materials an electronic charge density inhomogeneity does not diffuse at long wavelengths but instead excites plasmons, due to the long-range Coulomb interaction [7].

We realize the 2D Fermi Hubbard model using a degenerate spin-balanced mixture of two hyperfine ground states of ^{6}Li in an optical lattice. For details of the preparation scheme, see [23]. Our lattice beams produce a harmonic trapping potential, which leads to a varying atomic density in the trap. To obtain a system with uniform density, we flatten our trapping potential over a circular region of diameter 30 sites using a repulsive potential created with a spatial light modulator. We superimpose an additional sinusoidal potential that varies slowly along one direction of the lattice with a control-

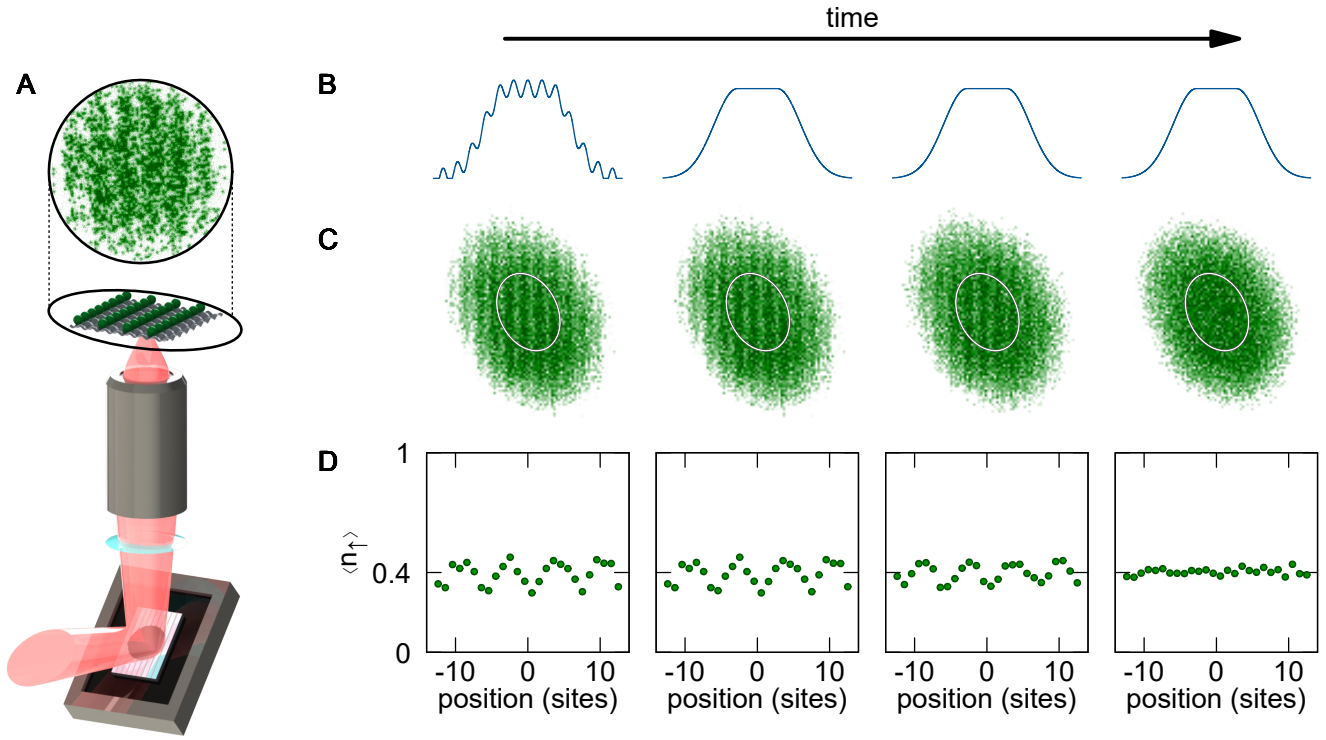

FIG. 1. **Measuring transport in the Hubbard model.** (**A**) Exemplary single shot fluorescence image of the atomic density for one spin component. Field of view diameter is ≈ 60 μm. Schematic representation of the setup for generating optical potentials. Far-off-resonant light is projected onto a digital micromirror device (DMD) and the resulting pattern is imaged onto the atoms using a high-resolution objective. We project a sinusoidally modulated potential along one direction. (**B**) One dimensional cuts along the projected potential. The DMD is used to flatten the trap and project a sinusoidally modulated potential (leftmost image). The confining potential comes from the optical lattice. After initial preparation, the sinusoidal potential is suddenly turned off, but the flattening potential is not. (**C**) Average density of a single spin component, $\langle n_\uparrow \rangle$, versus time for ≈ 30 images. Initially the system is in thermal equilibrium with a spatially modulated density (leftmost image). Immediately after the sinusoidal potential is turned off, the system is no longer in equilibrium but the density has not yet changed (second from left). The density modulation decays with time (third from left) until it is no longer visible (fourth from left). The central flattened region of the potential is marked by a white ellipse. The field of view is ≈ 75 μm $\times$ 75 μm. (**D**) Atomic density averaged along the direction orthogonal to the modulation in the central flattened region of the potential.

lable wavelength (Fig. 1A,B). By adiabatically loading the gas into these potentials, we prepare a Hubbard system in thermal equilibrium with a small amplitude (typically 10%) sinusoidal density modulation. Next, we suddenly turn off the added sinusoidal potential and observe the decay of the density pattern versus time (Fig. 1C,D), always keeping the optical lattice at fixed intensity. We measure the density of a single spin component, $\langle n_\uparrow \rangle$ using techniques described in [23], giving us access to the total density through $\langle n \rangle = 2 \langle n_\uparrow \rangle$.

We work at average total density $\langle n \rangle = 0.82(2)$. This value is close to a conjectured quantum critical point in the Hubbard model [24]. Our lattice depth is 6.9(2) E_r, where $E_R/h = 14.66$ kHz is the lattice recoil, leading to a tunneling rate of $t/h = 925(10)$ Hz. We adjust the scattering length, $a_s = 1070(10)a_o$, by working at a magnetic bias field of 616.0(2) G, in the vicinity of the Feshbach resonance centered near 690 G. These parameters lead to an on-site interaction to tunneling ratio $U/t = 7.4(8)$, which is chosen in the strong-coupling regime and near the value that maximizes antiferromagnetic correlations at half-filling [25].

We observe the decay of the initial sinusoidal density pattern over a period of a few tunneling times. The short timescale ensures that the observed dynamics are not affected by the inhomogeneous density outside of the central flattened region of the trap. To obtain better statistics, we apply the sinusoidal modulation along one dimension and average along the other direction (Fig. 1A,C). We fit the average modulation profile to a sinusoid, where the phase and frequency are fixed by the initial pattern (Fig. 2A). We plot the amplitude of the sinusoid versus time to quantify the decay of the density modulation, as in Fig. 2B.

We study the decay of the sinusoidal density pattern versus the wavelength of the modulation [26], and find that it becomes consistent with diffusive transport at long wavelengths. Diffusion predicts that the amplitude of a

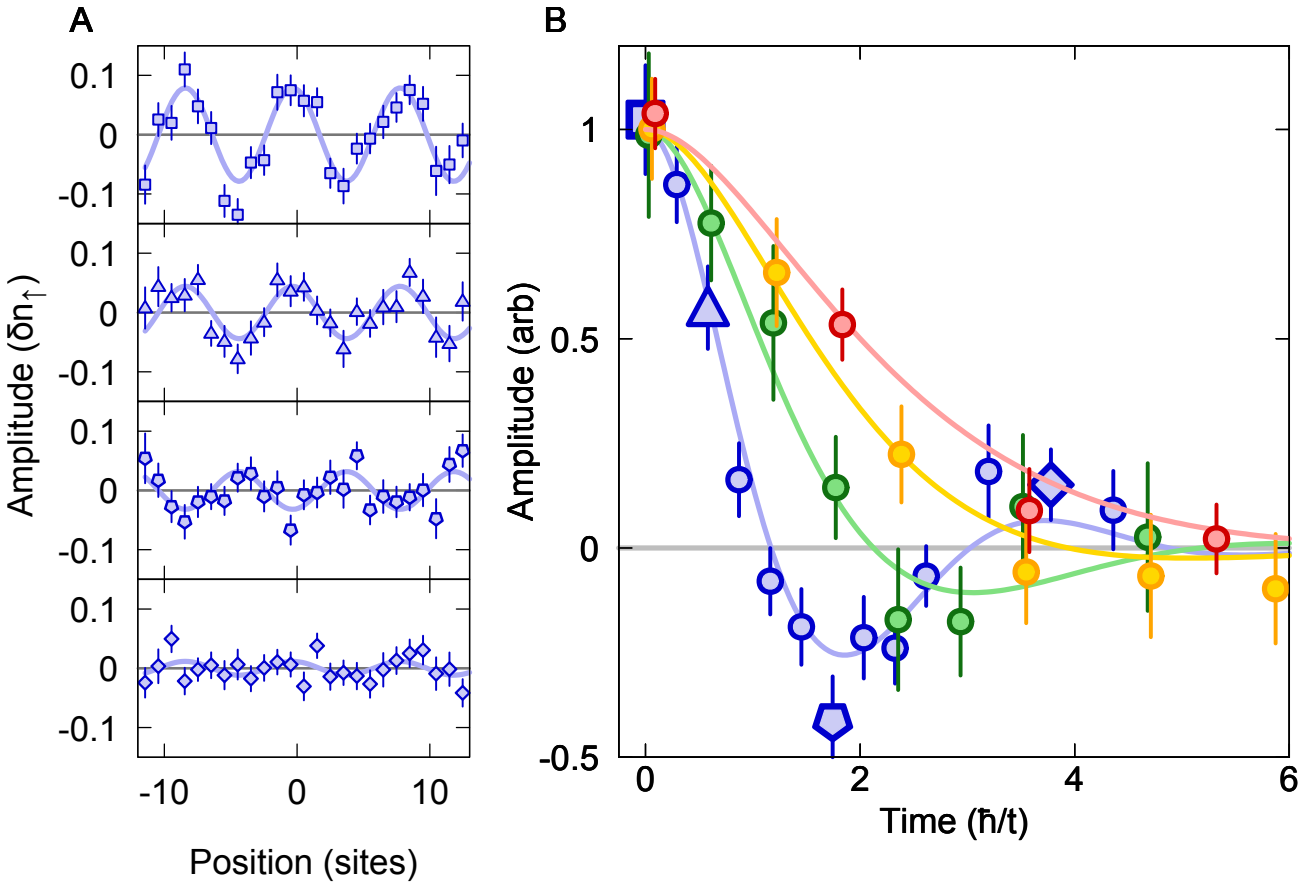

FIG. 2. **Decay of modulation pattern versus time.** (**A**) Cloud profiles averaged along the direction of the modulation (points) and sinusoidal fits (lines) for several different times and modulation wavelength 8.1 sites. The average value obtained from the sine fit has been subtracted. (**B**) Sinusoid fit amplitudes (points) versus decay time for modulation periods 8.1 (blue), 11.8 (green), 15.6 (yellow), and 18.7 (red) sites. Each curve is scaled by the initial modulation amplitude. Lines are obtained from a simultaneous fit of the diffusion constant, D, and momentum relaxation rate, Γ, to all wavelengths and times. Different shaped points for period 8.1 correspond to different panels in A, 0 $\hbar/t$ (square), 0.6 $\hbar/t$ (triangle), 1.7 $\hbar/t$ (pentagon), and 3.8 $\hbar/t$ (diamond). Error bars sem.

density pattern at wave vector $k = 2\pi/\lambda$ will decay exponentially with time constant $\tau = 1/Dk^2$, where D is the diffusion constant. We observe exponential decaying amplitudes with diffusive scaling for wavelengths longer than 15 sites. However, the decay curves are flat at early times, showing clear deviation from exponential decay. For short wavelengths, we observe deviations from diffusive behavior in the form of underdamped oscillations, which can be understood as the damped limit of sound waves. Both of these effects are related to the fact that it takes a finite amount of time to establish a particle current. This inertial effect is not described by the diffusion equation. To unify the description of modulation decay at all wavelengths, we developed a hydrodynamic description which accounts for conservation of density and a finite momentum (or current) relaxation rate [27]. This approach leads to a differential equation for the density decay,

$$\partial_t^2 n + \Gamma \partial_t n + \Gamma D k^2 n = 0,$$

where Γ is the momentum-relaxation rate and D is the diffusion constant. To determine these two parameters from our data at a fixed temperature, we simultaneously fit the amplitude as a function of time for all wavelengths with a common diffusion constant D and momentum relaxation rate Γ. An example of such a fit is shown in Fig. 2B. Our model neglects possible coupling between density and energy. We justify this approximation based on the empirical fact that our simple model fits the data and that we have not been able to detect any measurable temperature modulation in the gas [27]. In addition, theoretical work suggests that the thermopower (Seebeck coefficient) is negligible near our doping [13, 28].

We study the variation of the hydrodynamic parameters versus temperature by controlled heating of our cloud. After initial preparation of the cloud, we hold

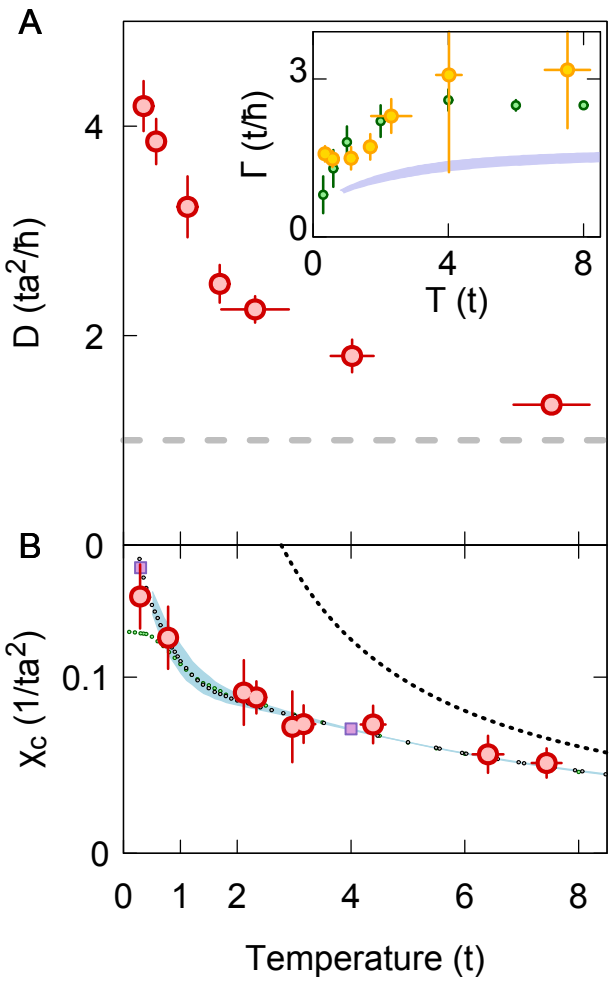

FIG. 3. **Hydrodynamic model parameters.** (**A**) Experimental diffusion constant, D, versus temperature (red) and Mott-Ioffe-Regel bound (grey). (**Inset**) Results for the momentum relaxation rate, Γ, including experimental data (yellow), single-site DMFT results for $\langle n\rangle = 0.825$ and $U/t = 7.5$ (green), and FTLM results on a 16-site cluster for $\langle n\rangle = 0.8 - 0.85$ and $U/t = 7.5$ (blue band). (**B**) Results for the charge compressibility, χ_c. Experimental results (red points), FTLM (blue band), DQMC at $\langle n\rangle = 0.83$ and $U/t = 7.5$ (grey points), single-site DMFT at $\langle n\rangle = 0.825$ and $U/t = 7.5$ (green points), cellular DMFT (purple squares), and the high-temperature limit $1/T$ scaling (black dashed line). Experimental error bars sem. For an explanation of the DMFT error bars, see [27].

the atoms in the trap or modulate the lattice amplitude for a controlled time to heat the system. To determine the temperature of the cloud after the system has equilibrated, we measure the singles density or local moment, $\langle n^s\rangle = \langle n_\uparrow + n_\downarrow - 2n_\uparrow n_\downarrow\rangle$, and the correlations between spin-up atoms $C^\uparrow(\mathbf{d}) = 4\left(\langle n_{\mathbf{i}+\mathbf{d},\uparrow} n_{\mathbf{i}\uparrow}\rangle - \langle n_{\mathbf{i}+\mathbf{d},\uparrow}\rangle \langle n_{\mathbf{i}\uparrow}\rangle\right)$, where $\mathbf{i} = (i_x, i_y)$. We compare these quantities to determinantal quantum Monte Carlo (DQMC) simulations to extract the temperature [27]. For temperatures at the low end of the range we can access, between $0.3 < T/t < 1$, the density correlations are a sensitive thermometer. At hotter temperature the singles density becomes a better thermometer. We have compared the temperature of the gas before switching off the potential modulation and after the density modulation has decayed, and find no measurable increase in the temperature of the gas.

We find that the diffusion constant, D, increases rapidly with decreasing temperature as shown in Fig. 3A. At high temperatures, D is expected to saturate, eventually approaching an infinite temperature limiting value [29]. As the temperature is lowered, Pauli blocking closes scattering channels, leading to an increased rate of diffusion. The Mott-Ioffe-Regel limit, which is a lower bound on the mean free path of a quasiparticle system, also provides a lower bound on the diffusion constant, $D \gtrsim ta^2/\hbar$. Our measured diffusion constants approach the MIR limit at high temperatures, but do not violate it. Due to the difficulty of measuring diffusion constants in materials, a direct test of the MIR limit in the strict mean-free-path sense has not been performed in real bad-metals. The diffusion constant is not directly accessible in exact theory as it requires working in the limit $\lambda \to \infty$ [27], and exact techniques such as diagonalization of finite systems and DQMC are limited to small system sizes. Even determining the infinite temperature limiting value is a non-trivial quantum dynamics problem [30, 31].

In a clean system like ours, momentum relaxation can only occur due to umklapp scattering, where the net momentum is not conserved in a collision but changes by a reciprocal lattice vector. We find that the momentum relaxation is strong at our interaction, leading to oscillations that are slightly underdamped for the shortest modulation wavelengths, and overdamped for the longer wavelengths. In this regime, our model is more sensitive to D than to Γ, as Γ drops out of the model entirely in the overdamped limit. We find the momentum relaxation rate, Γ, increases weakly with increasing temperature (Fig. 3, Inset). This trend may again be understood as Pauli-blocking suppressing momentum relaxation at low temperatures and becoming less important at higher temperatures. At the largest temperatures ($T/t \gtrsim 4$) we reach in this experiment Γ is difficult to extract because the modulation decay oscillations are nearly overdamped for all measured modulation periods. We compare the experimental Γ to results from finite-temperature Lanczos method (FTLM) and dynamical mean-field theory (DMFT) simulations by estimating the momentum relaxation rate as the half-width half-max of the Drude peak in the optical conductivity. The optical conductivity also has an additional peak at $\omega \sim U$, but this does not affect Γ significantly [27]. Our experimental Γ agrees reasonably with the DMFT results, but exceeds the FTLM results by up to a factor of two. FTLM is

an exact technique, and expected to give correct results at high temperature. One possible explanation for the discrepancy is that Γ is sensitive to the amplitude of the density modulation. To test this, we measured Γ and D versus modulation amplitude [27]. We found D is insensitive to the amplitude in the range explored. Γ shows some amplitude dependence but, due to the large error bars we can not conclusively say if this is the source of the discrepancy between experiment and FTLM.

We determine the charge compressibility in a separate experiment by measuring the variation of total density versus position in a harmonic trap and converting the position to chemical potential in the local density approximation [27, 32, 33]. The measured compressibility increases with decreasing temperature (Fig. 3B). For our hottest experimental temperatures, χ_c approaches $n(1-n/2)/T$, as expected in the high temperature limit [29]. At very low temperatures χ_c is expected to saturate, but we find no evidence of saturation down to $T/t = 0.3$. We compare our experimental results with DQMC, FTLM, and DMFT results. The DQMC and FTLM compressibilities agree well with the experimental data and do not saturate at low temperatures. In contrast, the single-site DMFT compressibility saturates at $T/t \approx 1$. The increasing compressibility below this temperature may be associated with short-range correlations [34], which are not accounted for by single-site DMFT. Cellular DMFT results using a 2×2 cluster agree with the DQMC compressibility, supporting this interpretation.

We use the Nernst-Einstein relation to determine the conductivity from the measured diffusion constant and charge compressibility (Fig. 4A). We examine the temperature dependence of the resistivity $\rho = 1/\sigma$ in Fig. 4B, and observe that it rises without limit, showing no sign of saturation. We estimate the MIR limit for resistivity, $\rho < \rho_{\mathrm{MIR}} \approx \sqrt{\frac{2\pi}{n}}\,(\hbar)$, and find our resistivity violates this bound for temperatures above $T/t \sim 1.3$. This behavior is similar to that observed in bad metals at high temperatures [6]. In this case, the violation of the MIR resistivity bound is not associated with the mean free path becoming shorter than the lattice spacing but rather with the temperature dependence of the compressibility [34]. We observe ρ exceeds the MIR limit near the Brinkman-Rice temperature scale, defined by $T_{\mathrm{BR}} = (1-n)W$, where $W = 8t$ is the bandwidth. Similar violation of the MIR limit at T_{BR} has been observed in DMFT studies [35, 36]. The Brinkman-Rice scale is an estimate of the degeneracy temperature of the quasiparticles in the doped Mott insulator.

To further elucidate the temperature dependence of ρ, we fit our results to the form $\rho(T) = \rho_o + AT + BT^2$. We find the temperature dependence is linear to good approximation as we obtain $\rho_o = 1.1(1)\hbar$, $A = 1.55(15)\frac{\hbar}{t}$, and $B = 0.03(3)\frac{\hbar}{t^2}$. Alternatively, a power law fit to the form $\rho(T) = \rho_o + (CT)^\alpha$ yields $\rho_o = 1.2(2)\hbar$, $C = 1.4(2)\frac{\hbar}{t}$, and $\alpha = 1.1(1)$. Similar fits show the inverse diffusion constant $1/D$ scales with $\alpha = 0.6(1)$ and the inverse charge compressibility scales with $\alpha = 0.85(20)$. In our temperature range, the linear resistivity is a combined result of the temperature dependence of the diffusivity and compressibility, both of which behave in a nontrivial way. This behavior should be contrasted with the high-temperature regime, $T \gg W$, where D saturates to a limiting value and the resistivity inherits its temperature dependence from the compressibility, which scales as $\chi_c \propto 1/T$ [29]. It should also be contrasted with the low-temperature regime usually considered in condensed matter where the compressibility has saturated and the resistivity inherits its temperature dependence from the diffusion constant.

At our hotter experimental temperatures we compare the measured resistivity with FTLM, which is an exact technique, and find reasonable agreement (Fig. 4). The experimental resistivity is systematically smaller than the FTLM calculation but within error bars. This may be a result of the uncertainty in determining U/t. At our coldest experimental temperatures, FTLM suffers from finite size effects which become relevant as correlation lengths approach the cluster size. For the 4×4 site cluster considered here, these effects limit FTLM resistivity calculations to $T/t \gtrsim 1$.

Because our experiment explores low temperatures which are inaccessible to FTLM, we also compare with an approximate technique, single-site DMFT [37] (Fig. 4). We find the DMFT tends to overestimate the experimental resistivity at high temperatures. At our hottest experimental temperatures, the DMFT resistivity is linear with a positive zero-temperature intercept. This linear scaling crosses over to a second linear scaling with a negative zero-temperature intercept around $T/t = 2$. This second linear region continues down to about $T/t = 0.8$ where the resistivity acquires a significant quadratic component. These regimes coincide with two different regimes observed in the DMFT compressibility (Fig. 3B). Previous DMFT studies at stronger interaction strengths have also observed these two linear regimes at intermediate temperatures, finding evidence for resilient quasiparticles in the lower temperature regime [35, 36]. We do not observe the predicted change of slope in the resistivity expected near $T/t = 2$ in either the experimental data (within uncertainties) or the FTLM results. This suggests a need for comparison between more refined DMFT techniques and exact techniques in the regime where this is possible.

Our experimental study of conductivity in the 2D Fermi-Hubbard model reveals linear scaling of the resistivity in the intermediate temperature regime and violation of the Mott-Ioffe-Regel resistivity bound at high temperatures through observations of previously unexplored Hubbard model hydrodynamics. We compare these results to state-of-the-art numerical techniques, in-

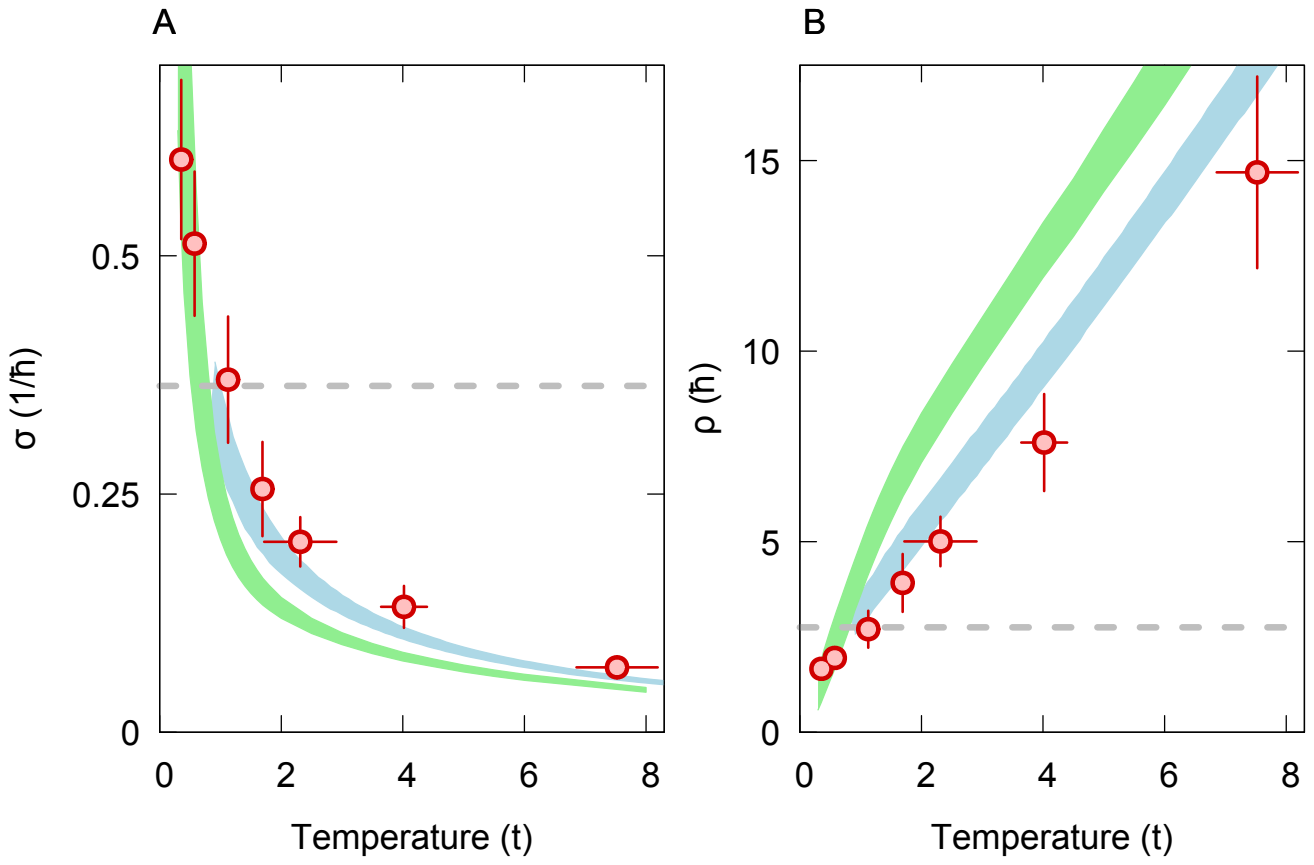

FIG. 4. **Conductivity versus temperature.** (**A**) Results for the DC conductivity, σ. Experiment (red), 16-site FTLM for $U/t = 7.5$ and $\langle n \rangle = 0.8 - 0.85$ (light-blue band), DMFT results for $U/t = 7.5$, $\langle n \rangle = 0.825$ (green band), and the Mott-Ioffe-Regel limit, $\sigma_{\mathrm{MIR}} = \sqrt{\frac{n}{2\pi}}\left(\frac{1}{\hbar}\right)$ (grey). (**B**) Results for the resistivity, ρ, using the same color scheme. Experimental error bars sem. For an explanation of the DMFT error band, see [27].

cluding an exact technique (FTLM) in the regime where this converges, and an approximate technique (DMFT) at lower temperatures. This experiment paves the way for future studies of the optical conductivity and thermopower, which can be examined near equilibrium using a similar approach. Both of these quantities might be expected to show anomalous scalings, as in the cuprates [4, 9]. In line with theoretical work such as [35, 36], searching for direct signatures of resilient quasiparticles using spectroscopic techniques [38] would also be very interesting. Further experimental studies will also provide important benchmarks for approximate theoretical methods, as the combination of low temperature, finite-doping, and dynamics is challenging for exact techniques.

We thank Joseph Thywissen, Martin Zwierlein, and Sean Hartnoll for stimulating discussions. We thank Charles-David Hébert, Maxime Charlebois, and Patrick Sémon for contributions to the continuous time Monte Carlo impurity solver codes. We thank Dominic Bergeron for assistance with the analytic continuation and comparison of results with the Two-Particle-Self-Consistent (TPSC) approach. This work was supported by the NSF (grant no. DMR-1607277), the David and Lucile Packard Foundation (grant no. 2016-65128), the AFOSR Young Investigator Research Program (grant no. FA9550-16-1-0269), the Canada First Research Excellence Fund, the Natural Sciences and Engineering Research Council of Canada (NSERC) under grant RGPIN-2014-04584, the Research Chair in the Theory of Quantum Materials (AMST), and the Slovenian Research Agency Program P1-0044. Simulations were performed on computers provided by the Canadian Foundation for Innovation, the Ministère de l'Éducation des Loisirs et du Sport (Québec), Calcul Québec, and Compute Canada. W.S.B. was supported by an Alfred P. Sloan Foundation fellowship. P.T.B. was supported by the DoD through the NDSEG Fellowship Program.

* wbakr@princeton.edu

[1] P. Coleman, *Introduction to Many-Body Physics* (Cam-

bridge University Press, 2015).
[2] A. Ioffe and A. Regel, Prog. Semicond. **4**, 237 (1960).
[3] N. F. Mott, Philos. Mag. **26**, 1015 (1972).
[4] N. E. Hussey, J. Phys.: Condens. Matter **20**, 123201 (2008).
[5] G. R. Stewart, Rev. Mod. Phys. **73**, 797 (2001).
[6] O. Gunnarsson, M. Calandra, and J. E. Han, Rev. Mod. Phys. **75**, 1085 (2003).
[7] S. A. Hartnoll, Nat. Phys. **11**, 54 (2014).
[8] P. W. Anderson, Phys. Rev. B **78**, 174505 (2008).
[9] C. M. Varma, P. B. Littlewood, S. Schmitt-Rink, E. Abrahams, and A. E. Ruckenstein, Phys. Rev. Lett. **63**, 1996 (1989).
[10] J. Vučičević, D. Tanasković, M. J. Rozenberg, and V. Dobrosavljević, Phys. Rev. Lett. **114**, 246402 (2015).
[11] S. A. Hartnoll, A. Lucas, and S. Sachdev, 1612.07324v2.
[12] D. J. Scalapino, "Handbook of high-temperature superconductivity," (Springer New York, 2007) Chap. Numerical Studies of the 2D Hubbard Model, pp. 463–493.
[13] J. Jaklič and P. Prelovšek, Adv. Phys. **49**, 1 (2000).
[14] J.-P. Brantut, J. Meineke, D. Stadler, S. Krinner, and T. Esslinger, Science **337**, 1069 (2012).
[15] G. Valtolina, A. Burchianti, A. Amico, E. Neri, K. Xhani, J. A. Seman, A. Trombettoni, A. Smerzi, M. Zaccanti, M. Inguscio, and G. Roati, Science **350**, 1505 (2015).
[16] S. Krinner, T. Esslinger, and J.-P. Brantut, J. Phys.: Condens. Matter **29**, 343003 (2017).
[17] M. Lebrat, P. Griins, D. Husmann, S. Husler, L. Corman, T. Giamarchi, J.-P. Brantut, and T. Esslinger, 1708.01250v2.
[18] H. Ott, E. de Mirandes, F. Ferlaino, G. Roati, G. Modugno, and M. Inguscio, Phys. Rev. Lett. **92**, 160601 (2004).
[19] N. Strohmaier, Y. Takasu, K. Günter, R. Jördens, M. Köhl, H. Moritz, and T. Esslinger, Phys. Rev. Lett. **99**, 220601 (2007).
[20] U. Schneider, L. Hackermüller, J. P. Ronzheimer, S. Will, S. Braun, T. Best, I. Bloch, E. Demler, S. Mandt, D. Rasch, and A. Rosch, Nat. Phys. **8**, 213 (2012).
[21] W. Xu, W. McGehee, W. Morong, and B. DeMarco, 1606.06669v4.
[22] R. Anderson, F. Wang, P. Xu, V. Venu, S. Trotzky, F. Chevy, and J. H. Thywissen, 1712.09965v1.
[23] P. T. Brown, D. Mitra, E. Guardado-Sanchez, P. Schauß, S. S. Kondov, E. Khatami, T. Paiva, N. Trivedi, D. A. Huse, and W. S. Bakr, Science **357**, 1385 (2017).
[24] N. S. Vidhyadhiraja, A. Macridin, C. Şen, M. Jarrell, and M. Ma, Phys. Rev. Lett. **102**, 206407 (2009).
[25] E. Khatami and M. Rigol, Phys. Rev. A **84**, 053611 (2011).
[26] S. Hild, T. Fukuhara, P. Schauß, J. Zeiher, M. Knap, E. Demler, I. Bloch, and C. Gross, Phys. Rev. Lett. **113**, 147205 (2014).
[27] Materials and methods are available as supplementary materials.
[28] G. Pálsson and G. Kotliar, Phys. Rev. Lett. **80**, 4775 (1998).
[29] E. Perepelitsky, A. Galatas, J. Mravlje, R. Žitko, E. Khatami, B. S. Shastry, and A. Georges, Phys. Rev. B **94**, 235115 (2016).
[30] S. Mukerjee, V. Oganesyan, and D. Huse, Phys. Rev. B **73**, 035113 (2006).
[31] E. Leviatan, F. Pollmann, J. H. Bardarson, D. A. Huse, and E. Altman, 1702.08894v2.
[32] T.-L. Ho and Q. Zhou, Nat. Phys. **6**, 131 (2009).
[33] E. Cocchi, L. A. Miller, J. H. Drewes, M. Koschorreck, D. Pertot, F. Brennecke, and M. Köhl, Phys. Rev. Lett. **116**, 175301 (2016).
[34] J. Kokalj, Phys. Rev. B **95**, 041110 (2017).
[35] X. Deng, J. Mravlje, R. Žitko, M. Ferrero, G. Kotliar, and A. Georges, Phys. Rev. Lett. **110**, 086401 (2013).
[36] W. Xu, K. Haule, and G. Kotliar, Phys. Rev. Lett. **111**, 036401 (2013).
[37] G. Kotliar, S. Y. Savrasov, K. Haule, V. S. Oudovenko, O. Parcollet, and C. A. Marianetti, Rev. Mod. Phys. **78**, 865 (2006).
[38] J. T. Stewart, J. P. Gaebler, and D. S. Jin, Nature **454**, 744 (2008).
[39] R. W. Floyd and L. Steinberg, Proc. Soc. Inf. Displays **17**, 75 (1976).
[40] L. P. Kadanoff and P. C. Martin, Ann. Phys. **24**, 419 (1963).
[41] B. S. Shastry, Rep. Prog. Phys. **72**, 016501 (2009).
[42] M. R. Peterson and B. S. Shastry, Phys. Rev. B **82**, 195105 (2010).
[43] L.-F. Arsenault, B. S. Shastry, P. Sémon, and A.-M. S. Tremblay, Phys. Rev. B **87**, 035126 (2013).
[44] J. Kokalj and R. H. McKenzie, Phys. Rev. B **91**, 205121 (2015).
[45] J. Kokalj and R. H. McKenzie, Phys. Rev. Lett. **110**, 206402 (2013).
[46] D. Poilblanc, Phys. Rev. B **44**, 9562 (1991).
[47] A. Georges and G. Kotliar, Phys. Rev. B **45**, 6479 (1992).
[48] G. Kotliar, S. Y. Savrasov, G. Pálsson, and G. Biroli, Phys. Rev. Lett. **87**, 186401 (2001).
[49] E. Gull, P. Werner, O. Parcollet, and M. Troyer, EPL **82**, 57003 (2008).
[50] P. Werner, A. Comanac, L. de' Medici, M. Troyer, and A. J. Millis, Phys. Rev. Lett. **97**, 076405 (2006).
[51] P. Werner and A. J. Millis, Phys. Rev. B **74**, 155107 (2006).
[52] K. Haule, Phys. Rev. B **75**, 155113 (2007).
[53] E. Gull, P. Werner, A. Millis, and M. Troyer, Phys. Rev. B **76**, 235123 (2007).
[54] P. Sémon, C.-H. Yee, K. Haule, and A.-M. S. Tremblay, Phys. Rev. B **90**, 075149 (2014).
[55] M. Caffarel and W. Krauth, Phys. Rev. Lett. **72**, 1545 (1994).
[56] L.-F. Arsenault and A.-M. S. Tremblay, Phys. Rev. B **88**, 205109 (2013).
[57] P. F. Maldague, Phys. Rev. B **16**, 2437 (1977).
[58] M. Calandra and O. Gunnarsson, EPL **61**, 88 (2003).
[59] C. N. Varney, C.-R. Lee, Z. J. Bai, S. Chiesa, M. Jarrell, and R. T. Scalettar, Phys. Rev. B **80**, 075116 (2009).

SUPPLEMENTARY MATERIAL

Methods

We work with an equal spin mixture of ^{6}Li hyperfine ground states $|1\rangle$ and $|3\rangle$, numbered up from the lowest energy state, which we label as spin up, $|\uparrow\rangle$, and spin down, $|\downarrow\rangle$, respectively. Our system is well described by the Fermi-Hubbard model with the Hamiltonian,

$$\mathcal{H} - \mu N = -t \sum_{\langle \mathbf{i},\mathbf{j}\rangle,\sigma} c^\dagger_{\mathbf{i},\sigma} c_{\mathbf{j},\sigma} + U \sum_{\mathbf{i}} n_{\mathbf{i},\uparrow} n_{\mathbf{i},\downarrow} - \mu \sum_{\mathbf{i},\sigma} n_{\mathbf{i},\sigma}, \tag{S1}$$

where $c^\dagger_{\mathbf{i},\sigma}$ is the creation operator for a fermion on site $\mathbf{i} = (i_x, i_y)$ with spin $\sigma \in \{\uparrow, \downarrow\}$, $n_{\mathbf{i},\sigma} = c^\dagger_{\mathbf{i},\sigma} c_{\mathbf{i},\sigma}$, t is the hopping rate, U is the on-site interaction, and μ is the chemical potential.

The experimental setup and basic parameters are described in detail in the supplement of ref. [23]. After preparing a 2D degenerate Fermi gas, we simultaneously load the optical lattice to a final depth of $6.9(2)\,\mathrm{E_r}$ and the sinusoidally modulated potential with a 50 ms intensity ramp. We then turn off the sinusoidal modulation in approximately 10 µs using the spatial light modulator and observe the decay of the density pattern.

We work at a field of 616.0(2) G. At this field and lattice depth, we find $U/t = 7.4(8)$ from a band structure calculation, which yields $t = 925(10)$ Hz, and spectroscopic measurement of $U = 7.0(7)$ kHz.

To prepare clouds of variable temperature, we use two different protocols. To reach temperatures in the range $T/t = 0.3 - 2$, we hold the cloud in the final trapping configuration for variable time. The gas heats due to technical noise at a rate of $3t$ per second. To reach even hotter temperatures, we modulate the lattice depth at a frequency of 2 kHz. To avoid losses, we perform this modulation at 595 G where the interaction is weaker. Finally, we ramp the field to its final value, turn on the DMD potential, and follow the same protocol as before.

For low temperatures, our lattice provides all of the radial confinement. For temperatures hotter than $T/t \approx 3$, the compressibility of the gas is reduced and we must provide extra confinement to reach appropriate filling. Therefore we increase our trapping frequency using a 1064 nm beam.

To image the density of a single spin state, we freeze the motion of the lattice by ramping the lattice depth to 60 E_R in approximately 100 µs. We checked that this ramp effectively freezes the atomic motion by comparing the measured amplitude modulation without turning off the DMD potential and with turning off the DMD potential and then immediately ramping the lattice depth for our shortest wavelength at our lowest temperatures (where the modulation decays fastest). The modulation depths agreed, indicating that the atomic motion is effectively frozen well before the lattice reaches 60 E_R.

DMD calibration

We engineer our deconfining and sinusoidally modulated potential using up to 15 mW of 650 nm coherent light derived from a tapered amplifier fed by a diode laser. Our spatial light modulator is a DLP Discovery 4100 with a DLP7000 digital micromirror device (DMD) in an imaging plane configuration. We image this light onto our atoms using two stages of demagnification. First, we demagnify the DMD image by a factor of 5, then we combine the DMD projection path with our imaging path on a dichroic mirror. Our imaging system demagnifies the light by an additional factor of 30. A single DMD micromirror has a pitch of 13.68 µm, so approximately 8×8 mirrors determine the potential at a single lattice site. Our imaging system spatially filters the binary image, resulting in a smooth potential at the atoms.

Before each experiment, we load a series of two images into the DMD memory. The first is the sum of a deconfining Gaussian potential for flattening the atomic density in the central part of the cloud with a sinusoidal modulation pattern. The second is only the deconfining potential. The DMD displays these images successively after receiving a trigger. We use the ALP-4.2 API "uninterruptible binary mode" to keep the image on the DMD until the next trigger. The DMD transitions between images in approximately 10 µs. During this time, all mirrors go to the off state, and then the mirrors needed for the next image are turned to the on state. The motion of the mirrors is underdamped, and we observe the mirrors bouncing by measuring diffracted light on a photodiode.

We produce binary images from continuous potential profiles using the Floyd-Steinberg error diffusion algorithm [39].

Hydrodynamic model

Hydrodynamics applies at long wavelengths and low frequencies when there are few conserved quantities, typically only mass, momentum, and energy. In most real materials, electrons cannot be treated hydrodynamically because of couplings to phonons and lattice defects which can absorb energy or momentum. For strongly interacting systems with no external couplings, hydrodynamics is applicable. In lattice systems the momentum is not conserved due to umklapp scattering, and only energy and particle number are conserved. In systems with weak enough umklapp (momentum relaxation) rate, we can also write down a "momentum conservation" equation with this relaxation rate. In the limit of strong momentum relaxation rate, this equation has no content. For a detailed discussion of when strongly interacting systems can be treated hydrodynamically, see [11].

The simplest hydrodynamic theory we can write down accounts for conservation of mass, weak relaxation of momentum, and assumes that energy is decoupled from these two. The two equations describing this are

$$\partial_t n(\mathbf{r},t) = -\nabla\cdot\mathbf{J}(\mathbf{r},t) \tag{S2}$$

$$\partial_t \mathbf{J}(\mathbf{r},t) = -\Gamma\left(D\nabla n(\mathbf{r},t) + \mathbf{J}(\mathbf{r},t)\right), \tag{S3}$$

where the first equation is the number conservation equation. The second equation can be viewed several ways. In one guise, it is the simplest differential equation that reduces to the diffusion equation when $\partial_t\mathbf{J}=0$. In another, it is the momentum "conservation" equation (Navier-Stokes equation) with a weak momentum relaxation rate Γ, and zero viscosity where we have neglected terms of higher order (e.g. terms that go like velocity squared) in linear response.

We spatially Fourier transform these equations and eliminate J to find,

$$\partial_t^2 n_k + \Gamma\partial_t n_k + \Gamma D k^2 n_k = 0, \tag{S4}$$

which is the equation that appears in the main text.

In the overdamped limit, $\Gamma \gg \sqrt{\Gamma D}k$, we recover diffusive behavior $n_k(t)\propto e^{-Dk^2t}$ for finite k. In the underdamped limit, we have sound-waves whose amplitude decays at rate $\Gamma/2$. If we take the limit $k=0$, the current decays exponentially at rate Γ, identifying this as the momentum relaxation rate. The sound-wave and current relaxation rates differ because the sound wave carries both kinetic and potential energy, shared equally, whereas the uniform ($k=0$) current excitation carries only kinetic energy. As only the kinetic energy is damped, the sound-wave loses energy at half of the rate of the uniform current excitation.

Linear response theory

To connect our hydrodynamic model for the density response of our Fermi-Hubbard system to quantities which can be calculated in theory, we consider the effect of perturbing our system with a time and spatial dependent potential, $v_{\mathbf{i}}(t) = F(t)\sin(\mathbf{k}\cdot\mathbf{r_i})$. In this experiment we suppose F is turned on slowly starting at $t=-\infty$ and switched off suddenly at $t=0$, leading to $F(t)=e^{\eta t}\theta(-t)$, where η parametrizes the slow turn on. If we suppose that H_o is the Fermi-Hubbard Hamiltonian in the absence of this, perturbation, then the full Hamiltonian is $H(t)=H_o+H'(t)$. We can write the perturbation term as

$$H'(t) = -\sum_{\mathbf{i}} v_{\mathbf{i}}(t) n_{\mathbf{i}} \tag{S5}$$

$$= -\sum_{\mathbf{k}} v_{\mathbf{k}}(t) n_{-\mathbf{k}}, \tag{S6}$$

where $\mathbf{r_i}$ is the position of site $\mathbf{i}$ and n_k is the spatial fourier transform of the density.

In linear response theory we think of v as the force which is conjugate to the density response. Given a Hamiltonian of the form in eq. S6, we can write the density reaction in terms of a response function Φ

$$\langle \delta n_{\mathbf{k}}(t)\rangle = \int_{-\infty}^{t} dt'\ \Phi(\mathbf{k},t-t') v_{\mathbf{k}}(t') \tag{S7}$$

$$\Phi(\mathbf{k},t-t') = -\frac{i}{\hbar}\Theta(t-t')\left\langle [n_{\mathbf{k}}(t), n_{-\mathbf{k}}(t')]\right\rangle, \tag{S8}$$

where we used translational invariance of the unperturbed system, which ensures that only $v_{\mathbf{k}}$ contributes to the density response at $\mathbf{k}$. This equation says that the response of the density to the applied field is given by the density correlations, encapsulated in the retarded Green's function Φ.

Fourier transforming eq. S7 in time and space leads to,

$$\langle \delta n_{\mathbf{k}}(\omega) \rangle = \chi(\mathbf{k}, \omega) v_{\mathbf{k}}(\omega) \tag{S9}$$

$$\chi(\mathbf{k}, \omega) = \int_{-\infty}^{\infty} dt' \; e^{i\omega t'} \Phi(\mathbf{k}, t') \tag{S10}$$

$$= -\frac{i}{\hbar} \int_{0}^{\infty} dt' \; e^{i(\omega + i\eta)t'} \Theta(t') \left\langle [n_{\mathbf{k}}(t'), n_{-\mathbf{k}}(0)] \right\rangle, \tag{S11}$$

where we added an small positive imaginary part, η, to the frequency so that the integral converges. We refer to $\chi(\mathbf{k}, \omega)$ as the density response function. χ is analytic in the upper-half plane, its real part is symmetric in ω, and its imaginary part is antisymmetric in ω.

Nernst-Einstein equation

In our experiment we have direct access to $\chi(\mathbf{k}, \omega)$ because we control the potential which is the generalized force that couples to the density. We want to measure the charge conductivity, σ, which is the response function for the current. The current is conjugate to the vector potential, which we do not control in this experiment. Fortunately, there is a general linear response formula which connects the density response function with the conductivity,

$$\sigma'(\omega) = \lim_{k \to 0} \frac{\omega}{k^2} \chi''(\mathbf{k}, \omega), \tag{S12}$$

where $\sigma'(\omega)$ is the real part of the conductivity and $\chi''(\mathbf{k}, \omega)$ is the imaginary part of the density response function.

To apply this expression, we need to know the form of χ. This is provided by our hydrodynamic model. Adding a force term to eq. S4 and using the definition of the response function from eq. S9 leads to the expression

$$\chi(\mathbf{k}, \omega) = \frac{\chi_c}{1 - \frac{i\omega}{k^2 D} - \frac{\omega^2}{k^2 D \Gamma}}, \tag{S13}$$

where χ_c is the charge compressibility, D is the diffusion constant, and Γ is the momentum relaxation rate [40]. Using this expression for χ in eq. S12 and taking the limit $\omega \to 0$ leads to the Nernst-Einstein relationship for the DC conductivity,

$$\sigma = \chi_c D. \tag{S14}$$

The Nernst-Einstein relation is a special case of eq. S12 which holds if the density has a diffusive mode at long times and large wave vectors. The Nernst-Einstein relation does not require the exact form for χ in eq. S13. We can, for example, add k^2-dependence to D or Γ.

Linearity

To assess the possibility of non-linear effects which are not included in our hydrodynamic model, we varied the initial amplitude of the density modulation at a fixed wavevector. For each curve, we fit a value for Γ and D, to test how the fitted model parameters change with amplitude. The amplitude versus time curves are shown in Fig. S1A for $\lambda \approx 12$ sites and temperature $T/t = 0.4(1)$. For each initial amplitude, we fit values for Γ and D using our hydrodynamic model. The fit results are shown in Fig. S1B,C. We find that the apparent Γ increases with increasing amplitude, and the apparent D is weakly effected by increasing amplitude. To establish an upper bound on the size of this effect, we perform a linear fit to the hydrodynamic parameters versus amplitude and extrapolate a 'zero-amplitude' value. We normalize the curve fit parameters by these values in Fig. S1B,C. Based on the statistical error in our fit lines, we find that at a typical experimental amplitude of $\delta n_{\uparrow} = 0.07$, Γ is increased by a factor of 1.4(4) and D by a factor of 1.06(10). Our extracted values for Γ appear to increase with amplitude, but the statistical error bar is quite large. This is due to the weak dependence of our model on the value of Γ. In the main text, we are able to obtain smaller error bars on Γ by simultaneously fitting decay curves at different modulation wavelengths. That approach is not feasible here because the degree of linearity may depend on modulation wavelength.

A related but distinct type of non-linearity is dependence of the charge compressibility on density. As the total density approaches half-filling, the compressibility decreases. Therefore, the chemical potential modulation we apply

tends to decrease the density at the minimum chemical potential values more than it increases the density at the maximum chemical potential values. This can lead to the density modulation deviating from a sine wave. At $T/t = 0.4$, the compressibility decreases by ≈ 20 % between $\langle n \rangle = 0.8 - 0.9$. At higher temperature, $T/t = 4$, the compressibility decreases by ≈ 2 %. We resolve this effect as a shift in the average density between the initial density modulation pattern and the long-time equilibrium density. This effect is largest at the coldest temperatures, and is at most $\delta n_\uparrow \approx 0.03$, which is comparable to the uncertainty in our density.

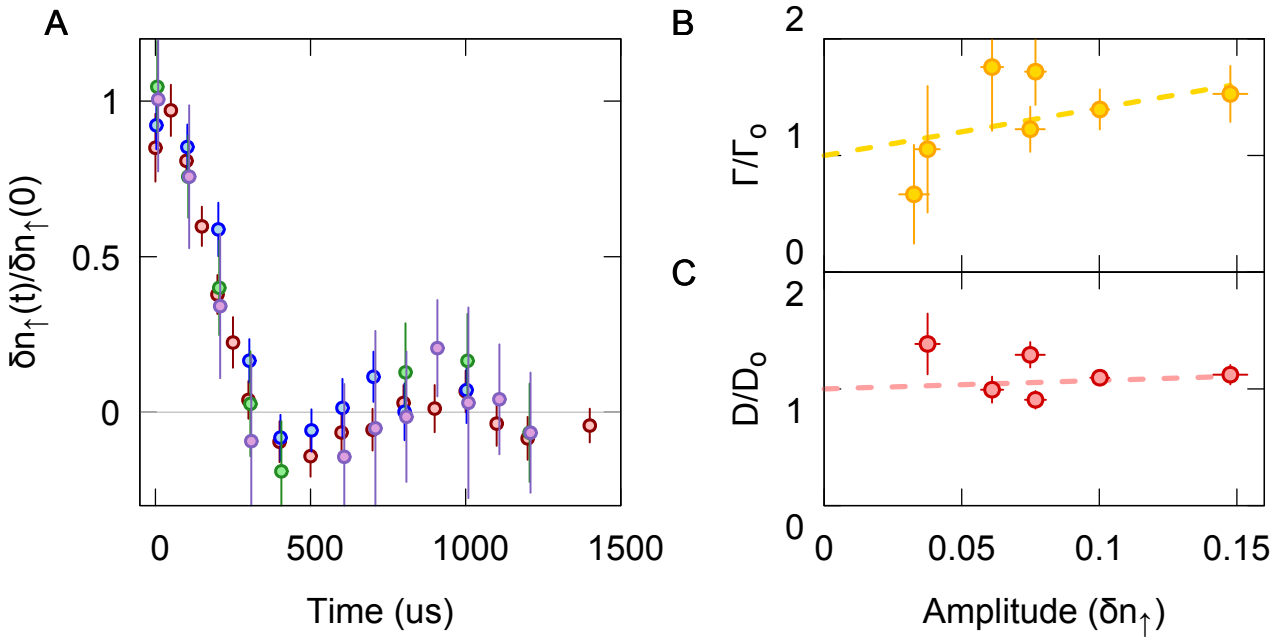

FIG. S1. **Linearity of the density response.** (**A**) Modulation amplitude versus decay time curves for selected initial amplitudes, $\delta n_\uparrow(t = 0) = 0.12$ (red), 0.08 (blue), 0.055 (green), and 0.035 purple. We see a collapse after scaling the curves to the initial modulation amplitude, $\delta n_\uparrow(0)$, obtained from a fit. (**B**) Variation in fit parameter Γ versus amplitude for the curves shown in a (red) and a linear fit to the results (dashed line). Γ is normalized by the extrapolated zero-amplitude value, Γ_o. (**C**) Variation in fit parameter D versus amplitude for the curves shown in a (red) and a linear fit to these results (dashed line). D is normalized by the extrapolated zero-amplitude value, D_o. Error bars sem.

Temperature fitting

We determine the temperature of our clouds by fitting to Determinantal Quantum Monte Carlo (DQMC) results. Spin resolved density $\langle n_\uparrow \rangle, \langle n_\downarrow \rangle$, correlation functions $\langle n_\uparrow(\mathbf{r}) n_\uparrow(0) \rangle_c$, and singles density $\langle n^s \rangle$ data is generated at $U/t = 8$ on a grid of chemical potentials and temperatures. The total density and correlation functions are then interpolated on a regular grid of density and temperature points.

We use these interpolating functions to simultaneously fit the singles density and the single-spin component correlations versus the total density. The only free parameter is the temperature. We apply an imaging fidelity correction of $f = 0.97$ based on our measured hopping and loss rates during imaging. An example fit is shown in Fig. S2.

Compressibility

We measure the compressibility of our gas in a harmonic trap with no additional potential provided by the DMD. For low temperatures, the lattice beams provide all the radial confinement, leading to $\bar{\omega} = (2\pi)185(10)$ Hz. For hotter temperatures, we use a circular beam to provide extra confinement, leading to $\bar{\omega} = (2\pi)280(10)$ Hz.

We determine the harmonic trapping frequencies by fitting the density and nearest-neighbor density correlation profiles of a weakly interacting gas obtained at a field of 568.0(1) G, near the noninteracting point of the $|1\rangle - |3\rangle$

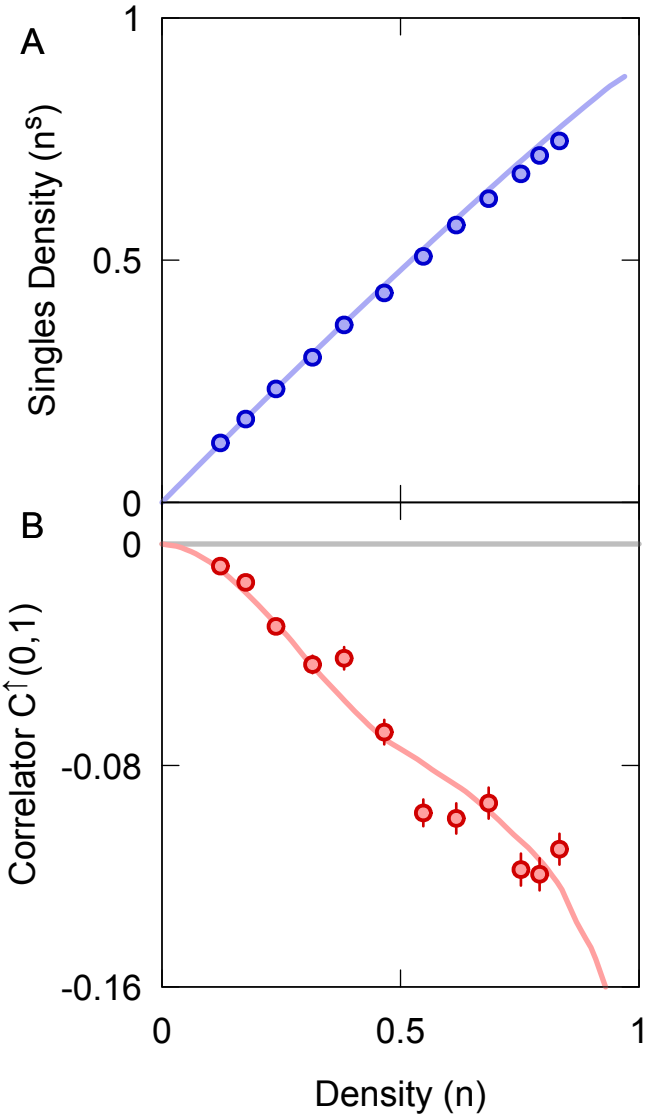

FIG. S2. **Temperature fitting.** (**A**) Experimental density versus singles density (points) and DQMC results (line). The DQMC results have been corrected for the experimental detection efficiency. This fit yields $T/t = 0.5(1)$. (**B**) Spin-up spin-up density correlator, $C^{\uparrow}(0,1)$, for nearest-neighbor sites. Error bars sem.

mixture, to the expected values for a non-interacting Fermi gas. These are determined from

$$n_{\uparrow} = \frac{1}{N}\sum_{\mathbf{k}} f(\epsilon_k - \mu, T) \tag{S15}$$

$$\frac{1}{4}C^{\uparrow}(\mathbf{d}) = -\frac{1}{N^2}\left|\sum_{\mathbf{k}} f(\epsilon_k - \mu, T)e^{-i\mathbf{k}\cdot\mathbf{d}}\right|^2, \tag{S16}$$

where $f(\epsilon, T)$ is the Fermi function, and $\mathbf{k}$ runs over the N allowed lattice momenta. Distance and energy scales are measured in units of the lattice constant and hopping respectively. We assume a harmonic trapping potential, $\mu(r) = \mu_o - \frac{1}{2}m\omega^2 r^2$ and fit our cloud profiles with μ_o, ω, and T as free parameters.

After determining the trapping frequency, we compute the compressibility according to,

$$\left(\frac{\partial n}{\partial \mu}\right)\Big|_T = -\frac{1}{m\omega^2}\left(\frac{1}{r}\frac{\partial n}{\partial r}\right). \tag{S17}$$

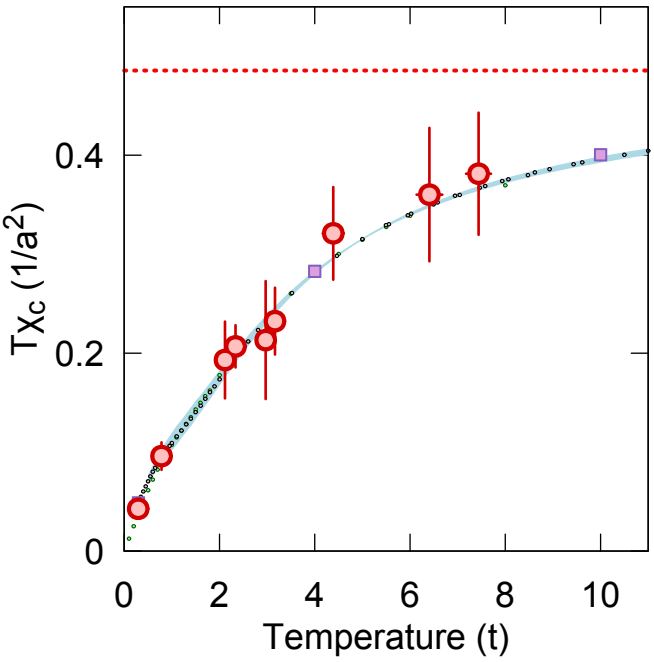

FIG. S3. **Compressibility.** Results for the charge compressibility times the temperature, $T\chi_c$. Experimental results (red points), FTLM (blue band), DQMC at $\langle n\rangle = 0.83$ and $U/t = 7.5$ (grey points), single-site DMFT at $\langle n\rangle = 0.825$ and $U/t = 7.5$ (green points), cellular DMFT (purple squares), and the high-temperature limit scaling $T\chi_c(T) = n(1-n/2)$ (red dashed line). Error bars sem.

Our cloud is slightly elliptic, with an aspect ratio of $\omega_x/\omega_y \approx 1.2$. Prior to determining the trapping frequency we perform an azimuthal average, which effectively rescales our coordinates $(x, y) \to \left(x\sqrt{\frac{\omega_x}{\omega_y}}, y\sqrt{\frac{\omega_y}{\omega_x}}\right)$. We measure r in these coordinates above, therefore our fitting procedures yields $\bar{\omega} = \sqrt{\omega_x\omega_y}$.

At high temperatures, the compressibility is expected to scale as $1/T$ with $T\chi_c(T) = n(1-n/2)$, for finite U [29]. We plot the compressibility times the temperature, $T\chi_c(T)$ in Fig. S3. $T\chi_c$ has not yet saturated in the temperature range considered here. We expect that saturation occurs at temperatures much hotter than the bandwidth, $T \gg 8t$.

Thermoelectric effects

We prepare our sample in thermal equilibrium, therefore there are initially no thermal gradients. However, thermal gradients may be generated during the subsequent dynamics. To check this possibility, we looked at a wave vector with underdamped oscillations at our lowest temperature. We measured nearest-neighbor correlations, $C^{\uparrow}(0,1)$, at the time where the amplitude first crosses zero. Here the density is flat, and any spatial variations in the correlator must be due to thermal gradients. We did not find any evidence for generation of thermal gradients.

Thermoelectric coupling is primarily due to two effects. The first is thermodynamic, and is described by the thermoelectric susceptibility, $\zeta = -\frac{\partial^2\Omega}{\partial\mu\partial T} = \frac{\partial n}{\partial T}\big|_{\mu} = \frac{\partial S}{\partial \mu}\Big|_{T}$, where $\Omega = \epsilon - ST - n\mu$ is the grand potential and S is the entropy. This is a static quantity, and can be computed, e.g., by FTLM. In the whole temperature regime accessible by FTLM we find $|\zeta| \lesssim 0.015t^{-1}$. This is small in the sense that generating a density gradient of $0.01a^{-1}$ requires a large temperature gradient of $\nabla T \approx 0.8ta^{-1}$.

The Seebeck coefficient is more difficult to calculate. Using the Mott-Heikes approximation [28, 41] or the Kelvin formula [42–44] gives a small Seebeck coefficient due to a maximum of entropy which occurs close to $\langle n\rangle \approx 0.83$. This is in agreement with previous observations using different models or techniques [13, 28]. A detailed description of particle diffusion in the presence of thermoelectric effects can be found in Ref. [7]. In the bad-metallic or high-T regime where the Kelvin formula is a good approximation for the Seebeck coefficient [42, 44], the effect of thermoelectric coupling on particle diffusion is negligible.

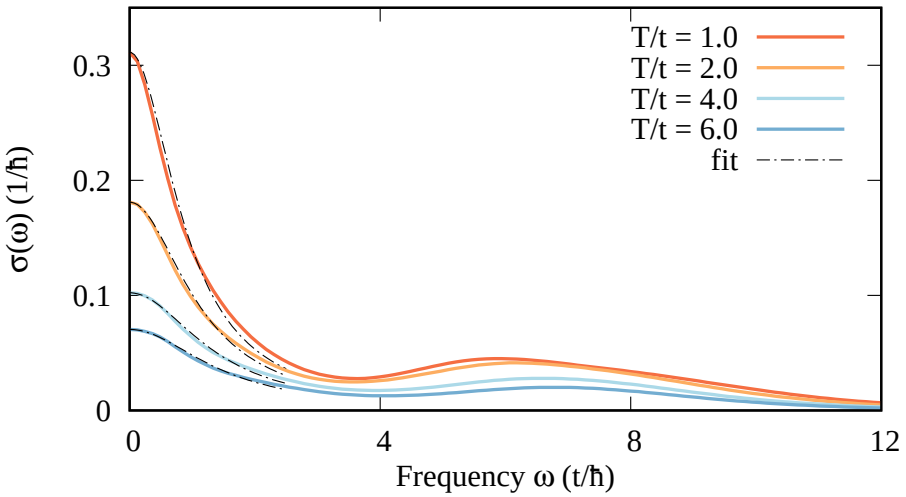

FIG. S4. **Optical conductivity** Real part of the optical conductivity $\sigma(\omega)$ for several T, $U = 7.5t$ and $n = 0.83$ as calculated with the FTLM on a 16 site cluster. With dashed black line a Lorentzian fit in the low frequency regime ($0 < \omega < 2.5t/\hbar$) is shown.

Determinantal quantum Monte Carlo (DQMC)

We perform DQMC calculations using the Quantum Electron Simulation Toolbox (QUEST) [59] on an 8×8 homogeneous square lattice. The inverse temperature is split into $L = 40$ imaginary time slices, where $L\Delta\tau = \beta$. We perform 5000 warm up sweeps, 50000 measurement sweeps and between 100 and 1000 passes to accumulate adequate statistics. We find that the sign problem at $\langle n \rangle = 0.83$ and $U/t = 7.5$ becomes important below $T/t = 0.5$. Reliable results in the range $T/t = 0.3 - 0.5$ can be obtained with additional statistics. Below $T/t = 0.27$, the sign approaches zero.

Finite-temperature Lanczos method (FTLM)

The finite-temperature Lanczos method (FTLM) [13, 45] is an exact diagonalization approach on small clusters (4×4 in our case). The method employs Lanczos diagonalization, which yields exact extremal eigenstates and effective or approximate eigenstates in the middle of the many-body spectrum. These states are together with the aid of the sampling over random initial vector used to calculate finite-T properties. Results have unwelcome finite size effects, which are large below some temperature $T_{\rm fs}$, but are negligible at $T > T_{\rm fs}$ due to shorter correlation lengths at high T. To reduce the finite size effects we employ averaging over twisted boundary condition [46] (with $N_\Theta = 64$ different boundary conditions) and summation over all symmetry sectors, e.g., we use grand canonical ensemble. We do not show FTLM results for $T < T_{\rm fs}$, which are potentially affected by finite size effects.

Dynamical quantities like the optical conductivity $\sigma(\omega)$ are calculated as correlation functions via evaluation of matrix elements of, e.g., the current operator, between the effective many body eigenstates, which are in this case obtained from two separate Lanczos procedures [13, 34]. The spectra, represented as a sum of weighted delta functions $\delta(\omega - \omega_i)$, needs to be further smoothed or broadened by η. Due to the exponential number of many body states and a very dense spectra, particularly at elevated T, the broadening can be relatively small and in our case $\eta \sim 0.1t \ll \Gamma$.

Optical conductivity (Fig. S4) for our parameters exhibit a Drude peak at low ω and separated Hubbard band at $\omega \sim U$. We fit the low-ω Drude peak to Lorentzian $\sigma_D(\omega) = \sigma/(1 + (\omega/\Gamma)^2)$, and extract the momentum relaxation rate Γ presented in the main text.

Dynamical mean-field theory (DMFT)

We describe the dynamical mean-field theory self-consistency loop and then the various impurity solvers used in this paper.

Self-consistency

Dynamical mean-field theory is exact in infinite dimension [47]. In finite dimension, it approximates the interacting problem by solving a self-consistent quantum impurity problem. A quantum impurity problem is the problem of a single site connected to an infinite bath of non-interacting electrons. The self-consistency is achieved by taking the same self-energy for both the quantum impurity problem and the lattice Green's function, and then requiring that the lattice Green's function projected on a single site equals the impurity Green's function. This takes into account both the localized physics of the atom and the itinerant character of the metal, in competition. When spatial correlations become important in low dimension, a cluster replaces the single site. The latter is known as Cellular Dynamical Mean-Field Theory (CDMFT) [48].

We describe the CDMFT procedure. Single site DMFT is a special case where the cluster is replaced by a single site. For the Hubbard Hamiltonian, defined in eq. S1, we write formally an effective action containing an hybridization function $\hat{\Delta}(\tau-\tau')$ that describes the degrees of freedom outside the cluster (the bath) as a time-dependent hopping within the cluster (which is easily pictured from a Feynman path integral point of view),

$$S_{\text{eff}} = \int_0^\beta d\tau d\tau' \Psi_d^\dagger(\tau) \left[(\partial/\partial\tau + \mu - \hat{t})\delta(\tau-\tau') - \hat{\Delta}(\tau-\tau') \right] \Psi_d(\tau') + U \sum_\mu \int_0^\beta d\tau n_{\mu\uparrow} n_{\mu\downarrow}. \tag{S18}$$

Hats denote matrices in the cluster degrees of freedom labeled by the greek letters μ, ν. Here, $\hat{t}$ is the hopping of the original Hamiltonian within the cluster. For the case of a 2×2 plaquette, the spinor is defined by $\Psi_d^\dagger \equiv (d_{1\uparrow}^\dagger, \ldots, d_{4\uparrow}^\dagger, d_{1\downarrow}^\dagger, \ldots, d_{4\downarrow}^\dagger)$. Physically, this action corresponds to a cluster embedded in a self-consistently determined medium.

Given the effective action with a starting guess for $\hat{\Delta}(\tau-\tau')$, the cluster propagator $\widehat{G}_c$ is solved with three methods: Two variants of continuous-time quantum Monte Carlo, and exact diagonalization, on which we comment further below. Once the cluster Green's function is obtained, we extract the cluster self energy from $\hat{\Sigma}_c = \hat{\mathcal{G}}_0^{-1} - \widehat{G}_c^{-1}$ where $\mathcal{G}_0^{-1}$ is the quantity in square brackets in the quadratic part of the action, while $G_{\mu\nu,\sigma} \equiv -\langle T d_{\mu\sigma}(\tau) d_{\nu\sigma}^\dagger(0)\rangle$ is the imaginary-time-ordered Green's function. Using the self-consistency condition in Matsubara frequency,

$$i\omega_n + \mu - \hat{t} - \hat{\Delta}(i\omega_n) = \left[\frac{N_c}{(2\pi)^2} \int d\widetilde{\mathbf{k}}\ \widehat{G}(\widetilde{\mathbf{k}}, i\omega_n) \right]^{-1} + \hat{\Sigma}_c(i\omega_n) \tag{S19}$$

with

$$\widehat{G}(\widetilde{\mathbf{k}}, i\omega_n) = \left[i\omega_n + \mu - \hat{t}(\widetilde{\mathbf{k}}) - \hat{\Sigma}_c(i\omega_n) \right]^{-1}, \tag{S20}$$

we recompute the hybridization function $\hat{\Delta}(i\omega_n)$ and iterate till convergence. Here $\hat{t}(\widetilde{\mathbf{k}})$ is the Fourier transform of the superlattice hopping matrix, N_c is the number of sites within the cluster and the integral over $\widetilde{\mathbf{k}}$ is performed over the reduced Brillouin zone of the superlattice.

Impurity solvers

The continuous-time quantum Monte Carlo solvers sample observables with a Markov chain defined in the space of Feynman diagrams of all orders. In the continuous-time auxiliary field method (CT-AUX) [49], the action is expanded in powers of the Hubbard interaction. This approach works better when U is less than the bandwidth. Expansion in powers of the hybridization function generates the so-called CT-HYB solver [50–52], which works better at values of U larger than the bandwidth [53]. For CT-HYB, we use a program that contains several improvements for speed [54]. The results are obtained from an average over the last 20 converged iterations and typically between 10^8 and 3×10^9 Monte Carlo updates. High frequency tails are usually of higher quality in the CT-AUX approach.

In the exact-diagonalization approach [55] that we used for single-site DMFT, the impurity problem is represented by an Anderson-like Hamiltonian $H_{\rm imp}$ with a discrete number of bath orbitals (here 5 for each spin component) coupled to the impurity

$$H_{\rm imp} \equiv \sum_{m\sigma} \epsilon_{m\sigma} a^\dagger_{m\sigma} a_{m\sigma} + \sum_{m\sigma} (V_{m\sigma} a^\dagger_{m\sigma} c_\sigma + \text{h.c.}) + U n_\uparrow n_\downarrow. \tag{S21}$$

Here, $m = 1...5$ for each spin component such that we have 10 bath energy levels $\epsilon_{m\sigma}$ coupled to the impurity via the bath-cluster hybridization matrix $V_{m\sigma}$. The hybridization function is obtained from

$$\Delta_\sigma(i\omega_n) = \sum_m \frac{V^2_{m\sigma}}{i\omega_n - \epsilon_{m\sigma}}. \tag{S22}$$

The parameters $\epsilon_{m\sigma}$ and $V_{m\sigma}$ are determined by imposing the self-consistency condition in Eq. S19 using a conjugate gradient minimization algorithm with a distance function

$$d = \frac{1}{N_{max}} \sum_{n=0}^{N_{max}} \left| \left(\hat{\mathcal{G}}_0'^{-1}(i\omega_n) - \hat{\mathcal{G}}_0^{-1}(i\omega_n) \right) \right|^2 \tag{S23}$$

where N_{max} is the largest Matsubara frequency index, determined by choosing a high-energy cutoff of about 2000 (energies are given in units of hopping t, and we take $\hbar = 1$ and $k_B = 1$). The distance function in Eq.(S23) is computed on the imaginary frequency axis since the hybridization function is a smooth function on that axis. We take a convergence criterion of 10^{-5} for the distance. We checked that the compressibility agrees with the continuous-time solvers to three significant digits.

Conductivity calculation

Since in single-site DMFT the vertex corrections vanish, the optical conductivity is calculated from the single-particle spectral weight using

$$\sigma'(\omega) = \frac{\chi''_{jj}(\omega)}{\omega} = \pi \sum_\sigma \int_{-4t}^{4t} \mathrm{d}\varepsilon \int \mathrm{d}\omega' \, \mathcal{T}(\varepsilon) \, \mathcal{A}(\varepsilon, \omega') \, \mathcal{A}(\varepsilon, \omega' + \omega) \times \frac{[f(\omega') - f(\omega' + \omega)]}{\omega}, \tag{S24}$$

where f is the Fermi-Dirac distribution, $\chi''_{jj}(\omega)$ is the imaginary part of the current response function, and $\mathcal{A}(\mathbf{k}, \omega)$ is the spectral function containing the non-interacting square-lattice dispersion $\varepsilon_{\mathbf{k}}$ and the impurity self-energy, and normalized so that $\int \mathrm{d}\omega \, \mathcal{A}(\mathbf{k}, \omega) = 1$. Here, the usual integral over wave-vectors has been replaced by an integral over the band energies ε weighted by the longitudinal transport function [56]

$$\mathcal{T}(\varepsilon) = \sum_{\mathbf{k}} \left(\frac{\partial \varepsilon_{\mathbf{k}}}{\partial k_x} \right)^2 \delta(\varepsilon - \varepsilon_{\mathbf{k}}) = -\frac{1}{2} \int_{-4t}^{\varepsilon} z N_0(z) \, \mathrm{d}z \tag{S25}$$

containing the non-interacting density of states N_0, normalized so that $\int N_0(z) \, \mathrm{d}z = 1$.

The real part of the conductivity obeys the f-sum rule in the following form [57]

$$\int \frac{d\omega}{\pi} \sigma'(\omega) = \frac{1}{N} \sum_{\mathbf{k}\sigma} \frac{\partial^2 \epsilon_{\mathbf{k}}}{\partial k_x^2} \langle n_{\mathbf{k}\sigma} \rangle = -\frac{1}{2} E_{kinetic}, \tag{S26}$$

where $\langle n_{\mathbf{k}\sigma} \rangle$ is the expectation value of the occupation number in state $\mathbf{k}\sigma$ and $E_{kinetic}$ is the expectation value of the kinetic energy for this two-dimensional system with nearest-neighbor hopping only. This means that even in situations where the optical conductivity is dominated by a Drude peak whose width is temperature independent, as in the range $4 < T < 8$ in the inset of Fig. 3, the DC conductivity can decrease with temperature because at high temperature the kinetic energy decreases as $1/T$ [58].

The exact diagonalization method, which is used to obtain the momentum relaxation rate and conductivity presented in the main text, allows one to obtain results directly on the real axis. However, the discrete nature of the bath introduces some uncertainty because the discrete energy levels must be broadened as Lorentzians of width η. When there is a range of η where the results are independent of η, one can be confident of the results. The error bars on the DMFT results in the main text correspond to the difference between $\eta = 0.1$ and a five times smaller value, $\eta = 0.02$. The estimate of of the momentum relaxation rate Γ is much less sensitive to η than the DC conductivity.